

Guided ultrasound calibration: where, how, and how many calibration fiducials

Elvis C. S. Chen¹ · Terry M. Peters¹ · Burton Ma²

Received: 29 January 2016 / Accepted: 16 March 2016 / Published online: 2 April 2016
© CARS 2016

Abstract

Purpose Many image-guided interventions rely on tracked ultrasound where the transducer is augmented with a tracking device. The relationship between the ultrasound image coordinate system and the tracking sensor must be determined accurately via probe calibration. **We introduce a novel calibration framework guided by the prediction of target registration error (TRE):** Between successive measurements of the calibration phantom, our framework guides the user in choosing the pose of the calibration phantom by optimizing TRE.

Methods We introduced an oriented line calibration phantom and modeled the ultrasound calibration process as a point-to-line registration problem. We then derived a spatial stiffness model of point-to-line registration for estimating TRE magnitude at any target. Assuming isotropic, identical localization error, we used the model to estimate TRE for each pixel using the current calibration estimate. We then searched through the calibration tool space to find the pose for the next fiducial which maximally minimized TRE.

Results Both simulation and experimental results suggested that TRE decreases monotonically, reaching an asymptote when a sufficient number of measurements (typically around 12) are made. Independent point reconstruction accuracy

assessment showed sub-millimeter accuracy of the calibration framework.

Conclusion We have introduced the first TRE-guided ultrasound calibration framework. Using a hollow straw as an oriented line phantom, we virtually constructed a rigid lines phantom and modeled the calibration process as a point-to-line registration. Highly accurate calibration was achieved with minimal measurements by using a spatial stiffness model of TRE to strategically choose the pose of the calibration phantom between successive measurements.

Keywords Ultrasound · Calibration · Spatial stiffness model · Target registration error · Fiducial localization error · Guidance · Virtual rigid lines phantom

Introduction and related work

Ultrasound (US) is ubiquitous in modern health care environment, providing information support by visualizing anatomy beneath the organ surface. It provides noninvasive real-time imaging without using ionizing radiation and is relatively inexpensive. One way to extend the utility of US into interventional medicine is to augment the US transducer with a spatial tracking device. In tracked US, a dynamic reference body (DRB) is rigidly attached to the US probe, allowing the pose (orientation and position) of the US image (or 3D volume for 3D US) and other tracked objects to be determined in a common coordinate system. The spatial relationship between the US image coordinate system to that of the DRB must be determined precisely through a process known as the probe calibration. In two review papers [13,20], every aspect of US calibration was thoroughly discussed, including the type of calibration phantom, their advantages and

✉ Elvis C. S. Chen
chene@roberts.ca

Terry M. Peters
tpeters@roberts.ca

Burton Ma
burton@cse.yorku.ca

¹ Roberts Research Institute, Western University,
London, ON, Canada

² Department of Electrical Engineering and Computer Science,
York University, Toronto, ON, Canada

disadvantages, effect of speed of sound (SoS) of the US coupling medium, and methods for accuracy assessment. To achieve the desired ultrasound calibration, consideration must be given to the costs (materials and construction) and the computational efforts (data collection and image processing) required.

One difficulty in achieving accurate US calibration is **fiducial localization error (FLE)** introduced by ultrasound physics, tracking uncertainty, inaccurate tool calibration, and fiducial segmentation error. For example, the accuracy of a point-based phantom [8,21] depends on how precisely the point fiducial can be placed in the ideal US mid-plane, and how well the fiducial can be localized in the calibration tool and the US image [13,22]. These problems can be mitigated by imaging the tool shaft instead of the tool tip and using the orientation of the shaft as the basis for US calibration [15]. This approach solves for the calibration through numerical optimization; hence, it is sensitive to initialization. For reliable optimization, the pixel scales need to be found explicitly and fixed before optimization [13,14]. Alternatively, an active echo element [11] can be used as a point source, allowing reliable and accurate identification of the ultrasound image mid-plane independent of the image quality as well as automatic point segmentation.

The z -phantom [6,7,10] is a wire-based fiducial designed to overcome the alignment problem. It comprises wires or rods arranged in coplanar z pattern which appear as collinear point fiducials in the US image. Multiple z -fiducials can be placed in different orientations and depths to increase the number of fiducials acquired per measurement; however, the z -phantom must be manufactured precisely, and the required image processing increases as the number of z -fiducials increases. Also, the configuration of the z -fiducials must be optimized for transducer geometry to accommodate US fan width and depth.

Categorically, both point-based (stylus or tool/needle tip) and z -fiducial phantoms are *oriented line fiducials*, where the position and the orientation of a line fiducial is specified by the end points of the tracked line. If isotropic scale is assumed, closed-form solutions can be obtained [1,12,23]. These solutions allow iteratively re-weighting of the data to mitigate the effect of statistical outliers [1,16]. We presented a numerical solution to solve point-to-point registration involving anisotropic scales [5], eliminating the need to pre-determine the scaling factors or assume isotropic scale.

A variation in the z -phantom was proposed by Welch et al. [24] who reformulated the calibration as a rigid body iterative closest point [3] (ICP) point-to-line registration. Their phantom consisted of multiple wires stretched taut between two parallel plates where the wires were not constrained to a z pattern, and the correspondences between US fiducials and lines were assumed. Their algorithm requires either pre-

terminated scales or the assumption of isotropic scale to solve the registration problem.

To obtain accurate calibration, it is important to scan the calibration phantom from a sufficiently diverse range of position, orientation, and its location spread throughout the B-mode image [13,20,22]. To the best of our knowledge, none of the US calibration algorithms in the current literature takes FLE into the consideration when deriving the numerical solution, nor do they provide real-time feedback as to where and how on the US image to measure the calibration phantom to achieve calibration robustly. A possible way to guide the calibration process is to optimize some measure of target registration error (TRE) in the US image plane, but TRE prediction has not yet been applied to the context of US calibration.

We previously presented an ICP-based US calibration method [4] using a single tracked straw. The process of US calibration is modeled as point-to-line registration where the correspondence between point (US fiducial) and line (tracked straw) is known explicitly. We now present the spatial stiffness model for this type of registration where, based on the current estimate of calibration parameter, the TRE for every US pixel can be estimated. This estimation provides a real-time feedback to the fitness of the calibration. We exhaustively search the calibration tool space to find the calibration fiducial pose that minimizes some measure of TRE. That is, we present a TRE-guided ultrasound calibration algorithm.

Materials and methods

An US calibration system was implemented, comprising custom software, an electromagnetic (EM) spatial tracker (Aurora, NDI, Canada), and a clinical US scanner (Sonix-Touch, Ultrasonix, Canada). A six degrees-of-freedom (DoF) EM DRB was rigidly attached to both the calibration phantom and US transducer (L14-5, Ultrasonix, Canada). US images were acquired digitally at a pixel count of 820×616 (width \times height). Standard imaging preset was used: abdomen, depth of 80 mm with a single focal point at 40 mm. Isotropic pixel scale was assumed to be 0.136 mm/pixel.

We previously described a hollow straw US calibration phantom (Fig. 1a and 1b) [2]. We demonstrated a hollow straw to be a suitable phantom material due to its echogenicity and symmetric appearance in a B-mode image acquired with a linear probe. Common materials used to construct calibration phantoms often produce hyperechoic reflection that is bright and blurred, with a shape and geometry that is not representative of the true cross section of the fiducial (Fig. 2). A solid plastic spherical point fiducial produces a crescent shape reflection due to low attenuation, whereas nylon wire and metallic needle both produce reflections that are larger

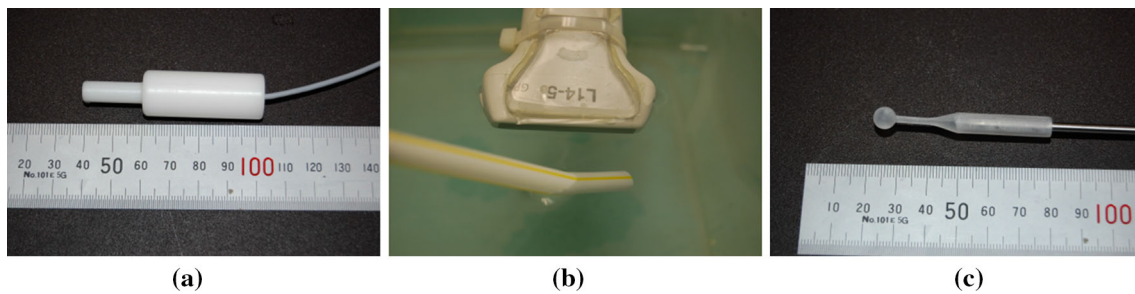


Fig. 1 Experimental setup: **a** physical dimensions of the straw phantom, **b** an Ultrasonix L14-5 linear probe submerged in room temperature water bath, and **c** a stylus with spherical tip for point reconstruction accuracy assessment

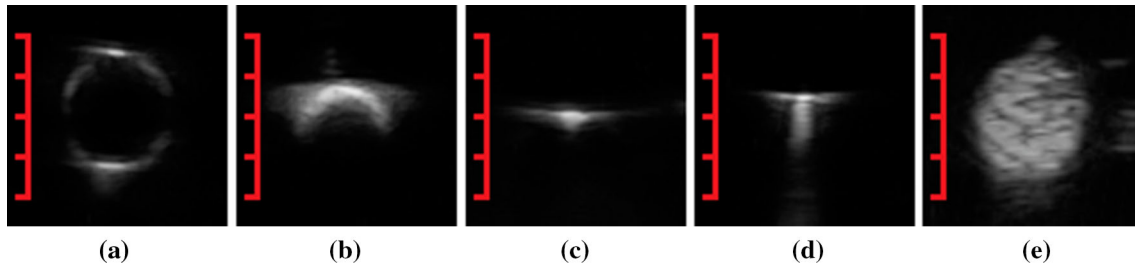


Fig. 2 Appearances of various types of fiducials: **a** a hollow straw (diameter=7.0 mm), **b** a solid plastic sphere (diameter=3.18 mm), **c** a taut braided nylon wire (diameter=0.3 mm), **d** a metallic needle tip

(24 G, diameter=0.51 mm), and (3) solid tube made with polyvinyl alcohol cryogel (diameter=7.0 mm). Each red tick mark is 2.5 mm

than the physical dimension of the line fiducial, with exaggerated reflection in both lateral and axial directions. A hollow sphere or a solid tube made with a low echogenic material (such as polyvinyl alcohol cryogel, Fig. 2e) would produce an elliptical reflection that is easy to segment, but practical considerations such as ease of construction and accurate tool calibration [25] remain as major engineering challenges. A hollow straw, on the other hand, always produces an elliptical reflection regardless of the angle of insonation. With the aid of a cross-hair cursor, the centroid of the elliptical reflection can be trivially and robustly identified. Automatic segmentation using the Hough Transform is possible, but we demonstrated that manual segmentation using visual aid is consistently more accurate than automatic segmentation [2].

The straw phantom comprises a 6-DoF DRB and a hollow straw, both attached to a concentric cylindrical base (Fig. 1a). The base can be manufactured precisely and inexpensively using a lathe. The axis of the cylindrical base, hence the orientation of the straw, can be calibrated to the attached DRB precisely by rotating it about a fixed axis. To alleviate the effect of tracking uncertainty, we advocate to image the section of the hollow straw that is closest to the attached DRB for each measurement of the calibration phantom.

Iterative closest point calibration and virtual rigid lines phantom

The process of US calibration is modeled as a special case of point-to-line ICP registration, where the correspondence

between points and lines is known explicitly. Each measurement of the straw phantom records the poses of the DRBs attached to the US transducer and the straw phantom, and the pixel location of the centroid of the elliptical US reflection (i.e., US fiducial). Let the subscripts $_{US}$, $_{pr}$, $_{s}$, and $_{w}$ denote the Cartesian coordinate system associated with US image, probe, straw phantom, and tracker (world), respectively. Without loss of generality, we assume the shaft of the straw phantom is aligned with the z -axis of the DRB (achieved via tool calibration). Let $p = [0, 0, a, 1; 0, 0, b, 1]^T$ be the end points of the straw phantom. Let:

$$p' = ({}^wT_{pr})^{(-1)}({}^wT_s)p \quad (1)$$

where ${}^wT_{pr}$ and wT_s are the recorded transforms of the DRB attached to the probe and straw phantom, respectively. Equation 1 specifies the pose of the straw fiducial in the local coordinate system of the probe DRB, where it is separated by one (i.e., US calibration) transform from the US pixel coordinate system.

Using the probe DRB as a reference coordinate system, all measurements of the straw phantom can be expressed in a common coordinate system using (1), producing a *virtual rigid lines phantom* (Fig. 3b). After a successful calibration, all the recorded US fiducials must coincide with all lines simultaneously. The point-to-line registration can be solved using ICP [3] if the pixel scale is isotropic or known a priori; otherwise, the anisotropic-scaled ICP [5] can be used to derive the calibration.

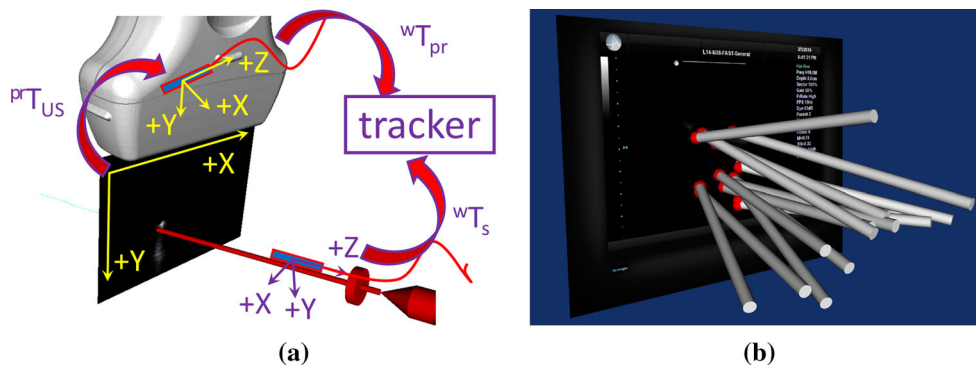


Fig. 3 Coordinate systems and transformation involved in US calibration: **a** both the ultrasound probe and a calibration phantom are spatially tracked; their poses (${}^wT_{pr}$ and wT_s) are measured relative to an external spatial tracking system. The spatial relationship between the US

image coordinate system to the probe DRB (${}^pT_{US}$) is the calibration transformation one seeks, and **b** representation of the *virtual rigid lines* phantom, constructed by concatenating all the recorded poses of the straw fiducial in a common coordinate system

Spatial stiffness model for point-to-line registration

A spatial stiffness model of point-to-line registration treats the registration points as a passive rigid mechanism suspended by linear springs. The springs change in length to exert a restoring force if the registration points are displaced. The amount of extension of the springs, and hence the energy stored in the springs, is determined by the FLE.

We assume that the N noise-free registration point locations $\{\mathbf{p}_1, \mathbf{p}_2, \dots, \mathbf{p}_N\}$, where $\mathbf{p}_j = [x_j \ y_j \ z_j]^T$, are known, and that each registration point \mathbf{p}_j lies on a line with known direction given by a unit direction vector \mathbf{n}_j (see left side of Fig. 4). We also assume that the 3D FLE for the j th registration point can be modeled as a zero-mean Gaussian variable with covariance matrix Σ_j where Σ_j is expressed in the same coordinate frame as the registration points.

The spatial stiffness matrix is derived by applying an infinitesimal rigid displacement to the mechanism and computing the Hessian of the potential energy stored in the linear springs. Let the rigid displacement be made up of a small rotation followed by a small translation. The small rotation is represented by a 3×3 rotation matrix $\mathbf{R} = \mathbf{R}_z(\omega_z)\mathbf{R}_y(\omega_y)\mathbf{R}_x(\omega_x)$ where $\mathbf{R}_x(\omega_x)$, $\mathbf{R}_y(\omega_y)$, and $\mathbf{R}_z(\omega_z)$

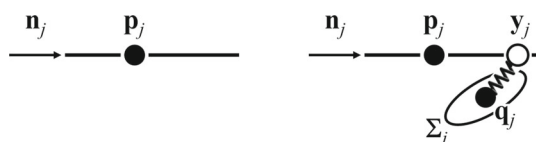


Fig. 4 Spatial stiffness model for point-to-line registration. (Left) a noise-free registration point \mathbf{p}_j on a line with unit direction vector \mathbf{n}_j . (Right) a noisy measurement of \mathbf{p}_j is modeled as the point $\mathbf{q}_j = \mathbf{R}\mathbf{p}_j + \delta$ obtained by rotation and translating \mathbf{p}_j by a small amount. The FLE noise is characterized by a covariance matrix Σ_j . The stiffness model uses a linear spring to connect \mathbf{q}_j to the point \mathbf{y}_j on the line that is closest to \mathbf{q}_j in terms of Mahalanobis distance

are the 3×3 rotation matrices representing rotations about the x -, y -, and z -axes by small amounts ω_x , ω_y , and ω_z , respectively. The translation is represented by the vector $\mathbf{t} = [t_x \ t_y \ t_z]^T$. The locations \mathbf{q}_j of the displaced registration points are given by $\mathbf{q}_j = \mathbf{R}\mathbf{p}_j + \mathbf{t}$.

Given a set of measured registration points $\{\mathbf{q}_1, \mathbf{q}_2, \dots, \mathbf{q}_N\}$ where each point has an FLE covariance matrix Σ_j , a solution to the registration problem can be obtained by minimizing the sum of squared Mahalanobis distances between the points \mathbf{q}_j and the lines $\mathbf{p}_j + t\mathbf{n}_j$. In the registration problem, the point \mathbf{p}_j that corresponds to \mathbf{q}_j is unknown and is usually inferred by finding the point \mathbf{y}_j on the line that is closest to \mathbf{q}_j in terms of Mahalanobis distance. The stiffness model uses the Mahalanobis distance between \mathbf{q}_j and \mathbf{y}_j as the change in length of the spring associated with \mathbf{q}_j (see Fig. 4); the potential energy stored in the spring associated with \mathbf{q}_j is

$$U_j = \frac{1}{2}(\mathbf{q}_j - \mathbf{y}_j)^T \Sigma_j^{-1}(\mathbf{q}_j - \mathbf{y}_j), \quad (2)$$

Computing the sum of the second-order partial derivatives of the U_j with respect to the translation and rotation parameters yields the stiffness matrix. We require an expression for the point \mathbf{y}_j on the line that is nearest to \mathbf{q}_j to compute the derivatives.

Mahalanobis distance between point and line

The point \mathbf{y}_j is the point that minimizes the Mahalanobis distance between the point \mathbf{q}_j having covariance matrix Σ_j and the line $\mathbf{p}_j + t\mathbf{n}_j$. The squared Mahalanobis distance between \mathbf{q}_j and \mathbf{y}_j is defined as:

$$D_M^2(\mathbf{q}_j, \Sigma_j; \mathbf{y}_j) = (\mathbf{q}_j - \mathbf{y}_j)^T \Sigma_j^{-1}(\mathbf{q}_j - \mathbf{y}_j) \quad (3)$$

To find an expression for \mathbf{y}_j , we can solve the following problem:

$$\arg \min_{\mathbf{y}_j} D_M^2(\mathbf{q}_j, \Sigma_j; \mathbf{y}_j) \quad \text{subject to} \quad \mathbf{y}_j = \mathbf{p}_j + t\mathbf{n}_j \quad (4)$$

Substituting the constraint into the objective function and expanding yields:

$$\begin{aligned} D_M^2(\mathbf{q}_j, \Sigma_j; \mathbf{y}_j) &= (\mathbf{q}_j - \mathbf{p}_j)^T \Sigma_j^{-1} (\mathbf{q}_j - \mathbf{p}_j) \\ &\quad - t(\mathbf{q}_j - \mathbf{p}_j)^T \Sigma_j^{-1} \mathbf{n}_j - t\mathbf{n}_j^T \Sigma_j^{-1} (\mathbf{q}_j - \mathbf{p}_j) + t^2 \mathbf{n}_j^T \Sigma_j^{-1} \mathbf{n}_j \end{aligned} \quad (5)$$

It is useful to make the substitution $\delta_j = (\mathbf{q}_j - \mathbf{p}_j)$ after which (5) simplifies to

$$D_M^2(\mathbf{q}_j, \Sigma_j; \mathbf{y}_j) = \delta_j^T \Sigma_j^{-1} \delta_j - 2t\delta_j^T \Sigma_j^{-1} \mathbf{n}_j + t^2 \mathbf{n}_j^T \Sigma_j^{-1} \mathbf{n}_j \quad (6)$$

Differentiating (6) with respect to t and equating to 0 yields:

$$t = t_0 = \delta_j^T \Sigma_j^{-1} \mathbf{n}_j / (\mathbf{n}_j^T \Sigma_j^{-1} \mathbf{n}_j) \quad (7)$$

which yields the desired expression for the nearest point:

$$\mathbf{y}_j = \mathbf{p}_j + t_0 \mathbf{n}_j = \mathbf{p}_j + (\delta_j^T \Sigma_j^{-1} \mathbf{n}_j / (\mathbf{n}_j^T \Sigma_j^{-1} \mathbf{n}_j)) \mathbf{n}_j \quad (8)$$

Note that the second derivative with respect to t of D_M^2 is the quadratic form $\mathbf{n}_j^T \Sigma_j^{-1} \mathbf{n}_j$ which is strictly positive for an invertible Σ_j ; thus, t_0 in (7) yields a local minimum of D_M^2 .

Spatial stiffness matrix for point-to-line registration

To derive the stiffness matrix for point-to-line registration, we substitute the nearest point \mathbf{y}_j given by (8) into the spring potential energy given by (2) and simplify:

$$U_j = \frac{1}{2} \left(\delta_j^T \Sigma_j^{-1} \delta_j - 2t_0 \delta_j^T \Sigma_j^{-1} \mathbf{n}_j + t_0^2 \mathbf{n}_j^T \Sigma_j^{-1} \mathbf{n}_j \right) \quad (9)$$

Substituting t_0 from (7) into (9) and simplifying yields:

$$U_j = \frac{1}{2} \delta_j^T \Sigma_j^{-1} \delta_j - \frac{1}{2} \frac{(\delta_j^T \Sigma_j^{-1} \mathbf{n}_j)^2}{\mathbf{n}_j^T \Sigma_j^{-1} \mathbf{n}_j} \quad (10)$$

The stiffness matrix is computed using the Hessian matrix of (10). More precisely, let U_j be a function of the vector \mathbf{u} where $\mathbf{u} = [t_x \ t_y \ t_z \ \omega_x \ \omega_y \ \omega_z]^T$ and then the symmetric 6×6 Hessian matrix \mathbf{H}_j is

$$\mathbf{H}_j = \begin{bmatrix} \frac{\partial^2 U_j}{\partial t_x^2} & \frac{\partial^2 U_j}{\partial t_x \partial t_y} & \cdots & \frac{\partial^2 U_j}{\partial t_x \partial \omega_z} \\ \frac{\partial^2 U_j}{\partial t_y \partial t_x} & \frac{\partial^2 U_j}{\partial t_y^2} & \cdots & \frac{\partial^2 U_j}{\partial t_y \partial \omega_z} \\ \vdots & \vdots & \ddots & \vdots \\ \frac{\partial^2 U_j}{\partial \omega_z \partial t_x} & \frac{\partial^2 U_j}{\partial \omega_y \partial t_x} & \cdots & \frac{\partial^2 U_j}{\partial \omega_z^2} \end{bmatrix} \quad (11)$$

The first term in (10) does not depend on the direction \mathbf{n}_j of the line and, in fact, is identical to the potential in the stiffness model of fiducial registration [18] where the points \mathbf{p}_j are fiducial marker locations; combining this observation with the linearity of differentiation, we can express the Hessian matrix as the difference $\mathbf{H}_j = \mathbf{H}_j^F - \mathbf{H}_j'$ where \mathbf{H}_j^F is the Hessian matrix for fiducial registration and \mathbf{H}_j' is the Hessian matrix computed using the second term in (10). The stiffness matrix \mathbf{K} is given by the sum of the N matrices \mathbf{H}_j evaluated at $\mathbf{u} = \mathbf{0}$. From [18], we have $\mathbf{H}_j^F|_{\mathbf{u}=\mathbf{0}} = \begin{bmatrix} \Sigma_j^{-1} & \Sigma_j^{-1} [\mathbf{p}]_{\times}^T \\ [\mathbf{p}]_{\times} \Sigma_j^{-1} & [\mathbf{p}]_{\times} \Sigma_j^{-1} [\mathbf{p}]_{\times}^T \end{bmatrix}$ where $[\mathbf{p}]_{\times} = \begin{bmatrix} 0 & -z_j & y_j \\ z_j & 0 & -x_j \\ -y_j & x_j & 0 \end{bmatrix}$ is the skew-symmetric cross-product matrix. Symbolic math software can be used to compute $\mathbf{H}_j'|_{\mathbf{u}=\mathbf{0}}$, but the resulting expressions are quite long; after simplifying, it can be shown that $\mathbf{H}_j'|_{\mathbf{u}=\mathbf{0}} = \frac{1}{\mathbf{n}_j^T \Sigma_j^{-1} \mathbf{n}_j} \begin{bmatrix} \Sigma_j^{-1} \mathbf{n}_j \\ \mathbf{p}_j \times \Sigma_j^{-1} \mathbf{n}_j \end{bmatrix} \begin{bmatrix} \Sigma_j^{-1} \mathbf{n}_j \\ \mathbf{p}_j \times \Sigma_j^{-1} \mathbf{n}_j \end{bmatrix}^T$. Finally, it is useful to partition the stiffness matrix into four 3×3 block matrices \mathbf{A} , \mathbf{B} , \mathbf{B}^T , and \mathbf{D} :

$$\mathbf{K} = \sum_{j=1}^N \mathbf{H}_j|_{\mathbf{u}=\mathbf{0}} = \sum_{j=1}^N \mathbf{H}_j^F|_{\mathbf{u}=\mathbf{0}} - \sum_{j=1}^N \mathbf{H}_j'|_{\mathbf{u}=\mathbf{0}} = \begin{bmatrix} \mathbf{A} & \mathbf{B} \\ \mathbf{B}^T & \mathbf{D} \end{bmatrix} \quad (12)$$

Identical isotropic noise case

If FLE noise is assumed to be identical and isotropic for all registration points, then it is the case that $\mathbf{H}_j^F|_{\mathbf{u}=\mathbf{0}} \propto \begin{bmatrix} \mathbf{n}_j \\ \mathbf{p}_j \times \mathbf{n}_j \end{bmatrix} \begin{bmatrix} \mathbf{n}_j \\ \mathbf{p}_j \times \mathbf{n}_j \end{bmatrix}^T$ which is the Hessian matrix for surface-based registration where \mathbf{p}_j is the location of a registration point and \mathbf{n}_j is the surface normal vector at \mathbf{p}_j [17]. The stiffness matrix for line-based registration can then be expressed as $\mathbf{K} = \mathbf{K}^F - \mathbf{K}^S$ which is the difference between the fiducial, \mathbf{K}^F , and surface-based, \mathbf{K}^S , registration stiffness matrices [19].

Estimating TRE for point-to-line registration

The stiffness matrix \mathbf{K} can be used to estimate the mean squared magnitude of TRE for any target location \mathbf{r} . The

background theory required to discuss the derivation of an expression for TRE magnitude is too long to repeat here, but has been previously described in great detail [18] (including a step-by-step summary of the necessary calculations). Briefly stated, the mean squared magnitude of TRE is given by

$$\text{TRE}^2(\mathbf{r}) = \sum_{i=1}^3 \left(\frac{1}{\sigma_i} + \frac{1}{\mu_{\text{eq},i}} \right) \quad (13)$$

where the σ_i , called the principal translational stiffnesses, determines the magnitude of TRE caused by translational displacement, and the $\mu_{\text{eq},i}$, called the principal rotational stiffnesses, determines the magnitude of TRE caused by rotational displacement. Both sets of principal stiffnesses are obtained by computing eigenvalues and eigenvectors of simple matrix expressions involving \mathbf{A} , \mathbf{B} , \mathbf{B}^T , and \mathbf{D} .

Fiducial localization error for oriented line fiducial

Even assuming perfect spatial tracking, the finite thickness of the US beam causes a hyperechoic signal of a fiducial before it reaches the ideal US mid-plane. Combined with uncertainty of fiducial segmentation, the FLE of a point phantom has three principal components: The FLE in plane (XY) of the US image is dominated by the uncertainty of fiducial segmentation, and FLE out of plane (Z) is dominated by the distance between the fiducial to the ideal US mid-plane (Fig. 5a). The in-plane FLE of point fiducial is further artificially magnified by imaging artifacts (Fig. 2).

Beam thickness has little effect on the out-of-plane FLE for a line fiducial because the full width of the fiducial intersects the US plane (Fig. 5b). The in-plane FLE is dominated by fiducial segmentation error caused by the nonuniform beam profile.

Due to the finite and varying thickness of the beam profile, we argue that, even with perfect segmentation of the ideal centroid of a circular/elliptical reflection, the true intersection of the point/line fiducial with the mid-plane is always biased toward the thin section of the image. Using the depiction in Fig. 5, as an example, if a line fiducial intersects the US image at the far field, the true intersection is always closer to the transducer than the ideal centroid of the reflection. The

amount of bias depends on the differential beam width as a function of the axial distance and thus cannot be quantified unless the beam profile is properly characterized.

A hollow straw produces an elliptical reflection; the thickness of the reflected straw wall increases as a function of the angle of insonation. In contrast to other solid and rigid phantom materials (Fig. 2), a tubular hollow straw produces an elliptical reflection whose symmetry is minimally impacted by the varying beam thickness. To obtain accurate centroid segmentation, we advocate manual segmentation using visual aid such as a cross-hair cursor, taking the axial bias into consideration.

Optimization heuristic strategies

We encapsulate the process of TRE prediction for point-to-line registration as:

$$\text{TRE} = \text{lineTRE}(P_{3 \times n}, N_{3 \times n}, S_{3 \times 3 \times n}, \text{tar}_{3 \times 1}) \quad (14)$$

where P is set of ultrasound fiducial coordinates, N is the direction of the oriented line, S is the noise covariance for each P , tar is the 3D location of the target, and the magnitude of TRE is computed using (13). Given n measurements of the calibration phantom, (14) returns the predicted scalar TRE for the specified target. To evaluate the fitness of current estimate of calibration, one can simply exhaustively evaluate TRE for every pixel using (14).

For the purposes of demonstrating the proposed algorithm, the noise covariance of FLE was assumed to be identical and isotropic, whose value was $\text{diag}([10, 10, 10])$ in pixel space. Such a value was chosen based on user experience; with a visual aid such as a cross-hair cursor, an experienced user can reliably identify the centroid of the elliptical reflection within a few pixels of uncertainty. We employed this isotropic and identical noise model because we do not have explicit knowledge of the true FLE for the point-to-line US calibration; however, the proposed TRE model handles the more general case of heteroscedastic FLE.

To guide US calibration, we exhaustively search the pose space (P_{n+1}, N_{n+1}) such that the predicted TRE using such additional measurement would maximally minimize the TRE

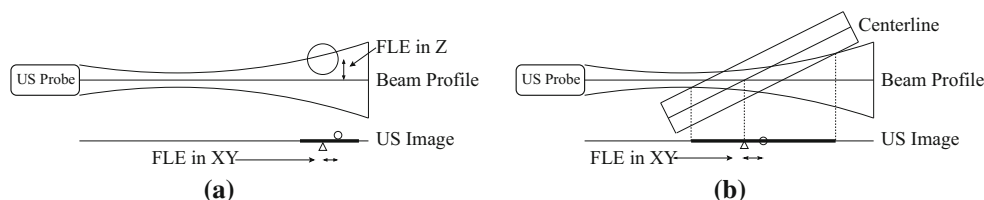


Fig. 5 Fiducial localization error due to finite thickness of US beam profile. Triangle denotes the true location of the fiducial; Circle denotes the centroid of the hyperechoic reflection. The out-of-plane FLE for

line fiducial is expected to be small compared to the in-plane FLE. The true intersection is always biased toward the focal region of the image. **a** Point fiducial. **b** Line fiducial

at the specified target location. The orientation, N_{n+1} , of the next line fiducial was chosen from nine different possible orientations, evenly spaced and within 45° from the normal of the US image. One strategy to obtain an accurate calibration for the entire US image is to specify a moving target between successive measurements, where the target to minimize TRE for is the least accurate pixel (has the highest TRE) based on the current calibration. On the other hand, there are clinical scenarios where the clinical target would always be located at a certain part of the US image (such as the jugular vein in central venous catheter insertion). For these application, one may wish to optimize US calibration specifically for a fixed target, such as the center of the US image.

Results

Custom software was implemented to facilitate US calibration and to visualize the predicted TRE. For each calibration tool measurement, the user is asked to manually identify the centroid of the elliptical reflection of the straw phantom. The calibration is bootstrapped with a minimum of four measurements, after which the TRE is evaluated at every single US pixel using (14). We then search the calibration tool pose space to collect the next fiducial such that the TRE at a specified target (Sect. 2.6) is maximally minimized. This process is repeated until the maximum TRE of the US image monotonically decreases to an asymptote.

Guided ultrasound calibration is aided by TRE visualization. An example pattern of calibration tool measurements is shown in Fig. 6 using the moving target strategy (Sect. 2.6).

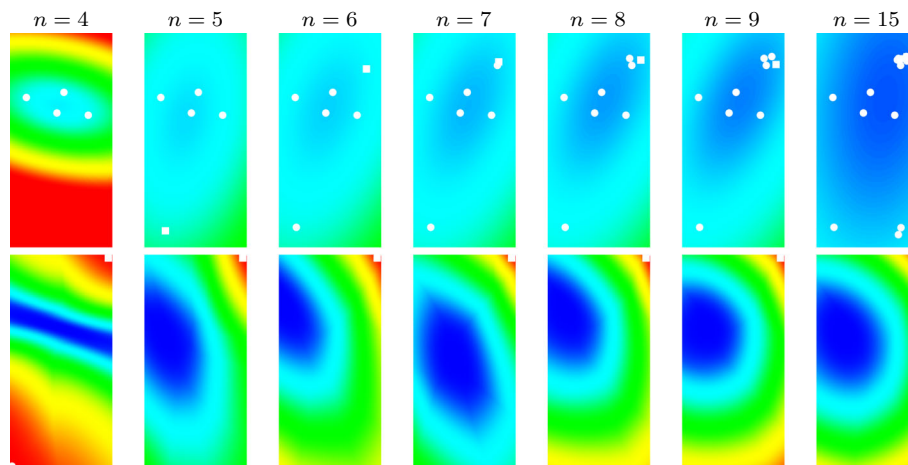


Fig. 6 TRE-guided ultrasound calibration visualization. (*Top row*) TRE of the image based on the current set of measurements. Circles are the existing fiducials; square is the newest additional fiducial. Orientation of the line fiducial is not shown. The blue \rightarrow red colormap depicts the range of $[0 - 20]$ TRE (in pixel). (*Bottom row*) TRE of a

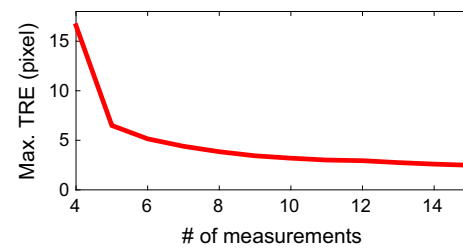
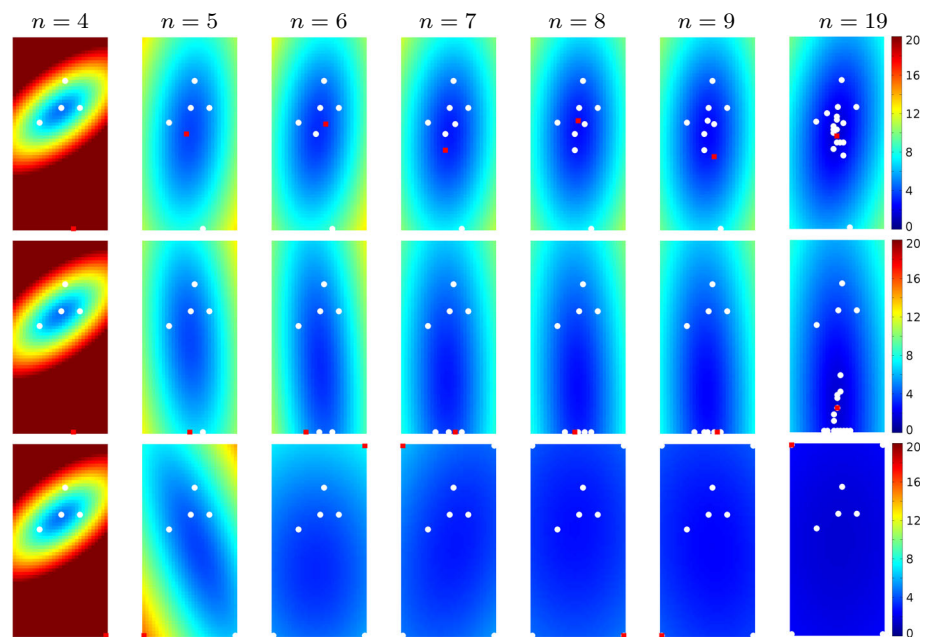


Fig. 7 Maximum TRE in the image plane as a function of the number of measurements for the calibration shown in Fig. 6. The TRE typically decreases monotonically until reaching an asymptote, reaching a stable calibration when more than 12 measurements were acquired

Four measurements were used to bootstrap the calibration where the fiducials were collected at the top of the US image (Fig. 6, top row, $n = 4$). The predicted TRE has an elliptical pattern where it is lowest in the region enclosed by the fiducials. The pixel with maximal TRE is located at the top-right corner of the image, the TRE of which can be maximally minimized if the next fiducial is to be measured at the bottom-left corner of the image (Fig. 6, bottom row, $n = 4$). Conversely, if one is to measure the subsequent fiducial in close proximity to the existing fiducial, it would have minimal impact on reducing TRE.

As the number of calibration tool measurements increases, the maximum TRE of the image decreases as there are more constraints to refine the calibration. For the calibration derived using data from Fig. 6, the TRE decreases monotonically, reaching an asymptote when more than 12 measurements were made (Fig. 7). The fitness of the calibration was evaluated independently using the point reconstruction accuracy [13,20] (PRA) metric. A tracked stylus with a spherical

Fig. 8 Simulation results for two different TRE minimization heuristics. Each figure displays the magnitude of predicted TRE at every point in the US image plane using the current set of registration points (shown as white circles). The red square shows the next-registration point chosen using the heuristic. (*Top row*) The next-registration point is chosen to minimize the TRE for a fixed target located at the center of the image plane. (*Middle row*) The next-registration point is chosen to minimize the TRE for a fixed target located slightly above the bottom center of the image plane. (*Bottom row*) The next-registration point is chosen to minimize the TRE at the point in the image plane that currently has the greatest TRE



silicone tip (Fig. 1c) was carefully calibrated and imaged by the calibrated US probe. The spherical tip was carefully placed into the US beam until it caused the largest and brightest reflection in the B-mode image. The centroid of the reflection was manually segmented by fitting a circle to the reflection. A total of 16 measurements were collected, and the PRA for the 16 points was 0.48 mm.

To highlight the differences in TRE minimization heuristics, three sets of simulations were performed. Assuming perfect tracking and tool measurements, Fig. 8 depicts the measurement patterns for three types of heuristics: fixed target at the center of the image (top row), fixed target at the bottom center of the image plane (middle row), and moving target for pixel that currently has the highest TRE. Each of these three heuristics was bootstrapped with the same calibration (based on four measurements). The magnitude of the predicted TRE always has an elliptical pattern, where it is lowest near the centroid of the fiducials. The pattern of measurements to minimize TRE are different between heuristics: For a fixed target, the suggested measurement will eventually coincide with the fixed target, whereas for a floating target the suggested measurements are along the periphery of the image. Although there appear to be repeated suggested measurement locations, the suggested direction of the line fiducial at a repeated location often changes.

Discussion and conclusion

We present an ultrasound calibration framework that is guided by the prediction of TRE using a new spatial stiffness model for point-to-line registration under heteroscedastic

noise. As far as we are aware, this is the first application of TRE prediction in the context of ultrasound calibration. Using TRE prediction, our framework provides strategies to guide where, how, and how many measurements to acquire in order to achieve accurate calibration. Both theoretical and experimental results suggest the accuracy of our framework increases monotonically, reaching a sub-millimeter asymptote when more than 12 measurements are acquired.

Calibration accuracy was 0.48 mm evaluated by the point reconstruction accuracy experiment. The metric PRA is an alternative presentation of the mean target registration error (mTRE), where, instead of multiple targets, a single stationary target is imaged by tracked US from various poses instead. In the calibration performed, the predicted TRE reached an asymptote of three pixels after sufficient number of measurements were acquired (Fig. 7). Assuming an isotropic pixel of 0.136 mm/pixel for our particular setup, the predicted TRE agreed closely with the observed PRA.

The proposed algorithm employs a hollow straw as the calibration tool, chosen based on its echogenicity and ease of segmentation. The use of a single straw calibration tool allows the construction of a virtual rigid lines phantom, encapsulating the process of ICP point-to-line registration. The virtual rigid lines phantom provides a mental model as how to constrain calibration by tool configuration. For example, measurements of the tool must be taken in an oblique and nonparallel configuration; otherwise, no unique calibration solution can be obtained.

The simulation results suggest that the isocontours of TRE for line-based registration are approximately elliptical, which is consistent with the results for fiducial registration (if the inertia tensor of the system treating the registration points as

point masses is constant for all N) [9, 18]. The point where TRE is minimized is approximately the centroid of the registration fiducials in the US image plane (it is not exactly equal to the centroid because the directions of the calibration fiducials and the FLE covariances also influence TRE magnitude). This observation explains the pattern of suggested registration point locations shown in Fig. 8. When minimizing the TRE for a fixed target location, the next-registration fiducial will be chosen so that the centroid of all of the fiducials in the US image plane will be near the target location. If the centroid of the fiducials is already nearly coincident with the target, then the only possible choices for the next fiducial location are near the target location; thus, the suggestions for the next fiducial location eventually converge on the target location. If we instead use a moving target, where the target location is taken to be the point on the image plane that has the greatest predicted TRE, then the target location will always coincide with one of the corners of the image plane (because of the ellipsoidal isocontours of TRE). To minimize TRE at a corner of the image, we must choose the next fiducial location near the same corner to shift the centroid of the fiducials closer to the corner. After adding the fiducial, the next target location will again be in one of the corners of the image; thus, the moving target heuristic will always suggest registration fiducials near the corners of the image.

The experimental results presented assumed an isotropic and identical FLE model, even though our proposed spatial stiffness model handles heteroscedastic FLE. Developing an accurate FLE model is difficult, since it depends on tracking uncertainty, US beam profile, tool calibration uncertainty, as well as segmentation uncertainty. As discussed in “Fiducial localization error for oriented line fiducial” section, the out-of-plane component of FLE for a hollow straw should be smaller than point or solid line fiducials. Such reduction in FLE may contribute to the low point reconstruction accuracy observed in our validation experiment. Tracker uncertainty in DRB attached to the line fiducial will contribute to the axial and lateral components of FLE in the US image. Tracker uncertainty in DRB attached to the US transducer will contribute primarily to the lateral component of FLE in the US image, with the magnitude increasing with the distance between the DRB and the point in the image. FLE caused by segmentation errors is expected to be small for our straw phantom because it always produces an elliptical reflection that can easily be segmented using a cross-hair cursor; however, segmentation error is likely to depend on user experience, with more experienced users able to localize a fiducial with higher precision. Incorporating all of these factors into a single FLE model and investigating the effect on ultrasound calibration accuracy is a possible area of future research.

We investigated the use of two different heuristics for minimizing TRE in the US image; however, there are many

alternative heuristics. One obvious type of heuristic is to minimize the average, median, or n -th percentile TRE over the entire image. Another type of heuristic is to minimize the average TRE for two or more targets. A particularly interesting idea is to combine the fixed and moving target ideas to jointly minimize the TRE at a fixed target and at the moving target coinciding with the point in the image having the current maximum TRE.

In summary, we have presented the first ultrasound calibration method that guides the user in choosing the pose of the calibration fiducial. By accounting for the general case of heteroscedastic FLE, our new spatial stiffness model iteratively proposes the next new pose for tool measurement such that the predicted TRE is maximally minimized. Using an inexpensive hollow straw as the calibration phantom, we virtually construct a rigid lines phantom and model the process of US calibration as a special case of ICP point-to-line registration. Both the theoretical and experimental results suggest our algorithm converges monotonically to a stable solution, reaching a sub-millimeter asymptote when sufficient measurements (typically around 12) are made. In a laboratory setting, calibration accuracy was 0.48 mm evaluated by an independent point reconstruction accuracy experiment.

Acknowledgments This study was funded by Canadian Institutes of Health Research (CIHR), Canada Foundation for Innovation (CFI), and Natural Sciences and Engineering Research Council of Canada (NSERC Discovery Grant).

Compliance with ethical standards

Conflict of interest Elvis C. S. Chen, Terry M. Peters, and Burton Ma declare that they have no conflict of interests.

Consent This article does not contain any studies with human participants or animals performed by any of the authors.

References

1. Ackerman M, Cheng A, Bector E, Chirikjian G (2014) Online ultrasound sensor calibration using gradient descent on the Euclidean group. In: Robotics and automation (ICRA), 2014 IEEE international conference on, pp 4900–4905
2. Ameri G, McLeod AJ, Baxter JSH, Chen ECS, Peters TM (2015) Line fiducial material and thickness considerations for ultrasound calibration. In: Proceedings of the SPIE, vol 9415
3. Besl P, McKay ND (1992) A method for registration of 3-D shapes. Pattern analysis and machine intelligence. IEEE Trans 14(2):239–256
4. Chen EC, McLeod AJ, Baxter JS, Peters TM (2015) An iterative closest point framework for ultrasound calibration. In: Augmented environments for computer-assisted interventions, vol 9365, Springer International Publishing, pp 69–79
5. Chen EC, McLeod AJ, Baxter JS, Peters TM (2015) Registration of 3D shapes under anisotropic scaling. Int J Comput Assist Radiol Surg 10(6):867–878

6. Chen TK, Thurston AD, Ellis RE, Abolmaesumi P (2009) A real-time freehand ultrasound calibration system with automatic accuracy feedback and control. *Ultrasound Med Biol* 35(1):79–93
7. Comeau RM, Fenster A, Peters TM (1998) Integrated MR and ultrasound imaging for improved image guidance in neurosurgery. In: *Proceedings of the SPIE*, vol 3338, pp 747–754
8. Detmer PR, Bashein G, Hodges T, Beach KW, Filer EP, Burns DH, Strandness DE Jr (1994) 3D ultrasonic image feature localization based on magnetic scanhead tracking: in vitro calibration and validation. *Ultrasound Med Biol* 20:923–936
9. Fitzpatrick J, West J, Jr Maurer CR (1998) Predicting error in rigid-body point-based registration. *Med Imaging IEEE Trans* 17(5):694–702
10. Gower JC, Dijksterhuis GB (2004) *Procrustes problems*. Oxford University Press, Oxford
11. Guo X, Cheng A, Zhang H, Kang HJ, Etienne-Cummings R, Bector E (2014) Active echo: A new paradigm for ultrasound calibration. In: *Medical image computing and computer-assisted intervention*, Springer, pp 397–404
12. Horn BK (1987) Closed-form solution of absolute orientation using unit quaternions. *J Opt Soc Am* 4:629–642
13. Hsu PW, Prager RW, Gee AH, Treece GM (2009) Freehand 3D ultrasound calibration: a review. In: *Advanced imaging in biology and medicine*, Springer, Berlin, pp 47–84
14. Hsu PW, Treece GM, Prager RW, Houghton NE, Gee AH (2008) Comparison of freehand 3-D ultrasound calibration techniques using a stylus. *Ultrasound Med Biol* 34(10):1610–1621
15. Khamene A, Sauer F (2005) A novel phantom-less spatial and temporal ultrasound calibration method. In: *Medical image computing and computer-assisted intervention*, Springer, pp 65–72
16. Ma B, Ellis RE (2003) Robust registration for computer-integrated orthopedic surgery: laboratory validation and clinical experience. *Med Image Anal* 7(3):237–250
17. Ma B, Ellis RE (2004) Spatial-stiffness analysis of surface-based registration. In: *Medical image computing and computer-assisted intervention*, Springer, pp 623–630
18. Ma B, Moghari M, Ellis R, Abolmaesumi P (2010) Estimation of optimal fiducial target registration error in the presence of heteroscedastic noise. *Med Imaging IEEE Trans* 29(3):708–723
19. Ma B, Peters TM, Chen ECS (2016) Estimation of line-based target registration error. *Proc SPIE* 9786:978626-1–978626-9
20. Mercier L, Langø T, Lindseth F, Collins LD (2005) A review of calibration techniques for freehand 3-D ultrasound systems. *Ultrasound Med Biol* 31(2):143–165
21. Muratore DM, Galloway RL Jr (2001) Beam calibration without a phantom for creating a 3-D freehand ultrasound system. *Ultrasound Med Biol* 27(11):1557–1566
22. Prager RW, Rohling RN, Gee AH, Berman L (1998) Rapid calibration for 3-D freehand ultrasound. *Ultrasound Med Biol* 24(6):855–869
23. Schönemann PH (1966) A generalized solution of the orthogonal procrustes problem. *Psychometrika* 31(1):1–10
24. Welch J, Bax M, Mori K, Krummel T, Shahidi R, Maurer C (2002) A fast and accurate method of ultrasound probe calibration for image-guided surgery. In: *Proceedings of computer assisted radiology and surgery*, p 1078
25. Yaniv Z (2015) Which pivot calibration? In: *Proceedings of the SPIE*, vol 9415